sinus rhythm. All patients gave informed consent for an electrophysiologic study, catheter ablation, and CT. As a control group, CT also was performed in 14 subjects with neither a history of AF nor structural heart disease (10 men, 4 women; mean age, 57 ± 16 years).

Electrophysiologic Study and Catheter Ablation

PV isolation was performed as previously described.[1,2,8] Electrograms were recorded near the PV ostia with a 7 Fr decapolar ring catheter (Lasso, Biosense Webster, Inc., Diamond Bar, CA, USA). RF energy was delivered with a 7 Fr quadripolar ablation catheter with a 4 mm distal electrode. PV isolation was performed by applying RF energy at the sites at which the earliest bipolar PV potentials and/or unipolar electrograms with the most rapid intrinsic deflection were recorded.[1,2,8] RF energy was delivered at a maximum power of 30 W and maximum temperature of 52°C–55°C for 60 seconds.[1,2,8] The endpoint for ablation was the elimination of the PV potentials at all Lasso catheter recording sites.

Multi-Slice CT

The images were acquired using a multi-slice CT scanner (GE Light Speed Ultra; GE Medical Image, Milwaukee, WI, USA) during intravenous injection of contrast dye (100 mL at 3 mL/s) in eight parallel slices (1.25 mm collimation). ECG gating was performed with a triggered delay set at 70% of the R-to-R interval to target the atrial end-diastolic phase. A processing workstation (Advanced Workstation 4.0; GE Medical Image) allowed for three-dimensional viewing of curved multi-planar reconstruction (MPR) images (Fig. 1A and B), virtual endoscopic images, reformatted cross-sectional images in discretionary directions (Fig. 1C), and volume rendering images (Figs. 2, upper panels, and 3). Curved MPR images were obtained using a cursor to trace a curved line along the center of the lumen of the PV manually on

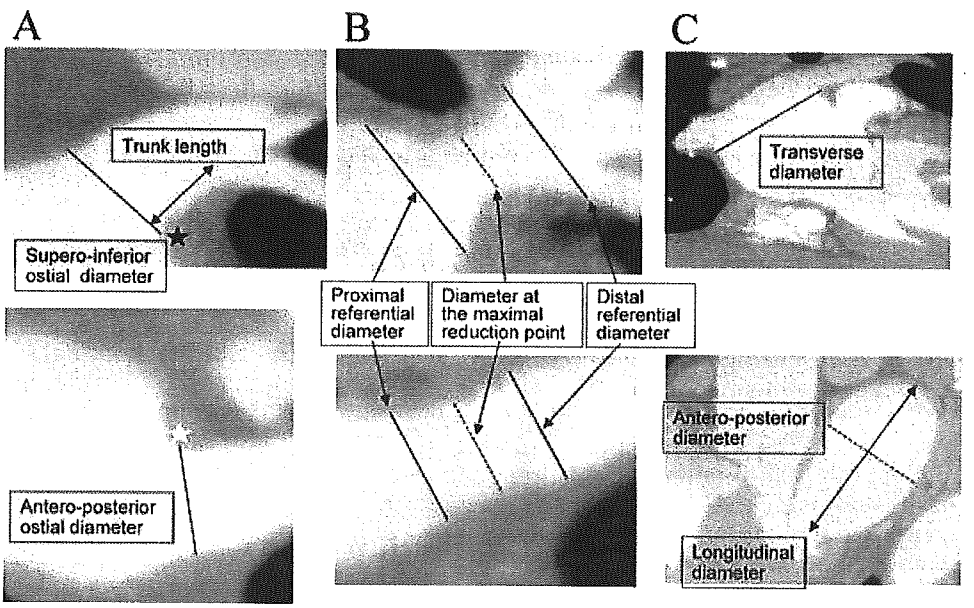

Figure 1. *(A) Measurement of the ostia of the pulmonary veins (PV) with curved MPR (upper panel: integrated coronal sectional view) and axial (lower panel: integrated axial sectional view) images of the left superior PVs. The black asterisk identifies the apex of the parabolic outline of the junction of the intervenal bridging wall. The trunk length of the PV was defined as the distance between the ostium and the onset of the first branch of the PV (arrow). The white asterisk identifies the apex of the parabolic outline of the junction to the left atrial appendage. (B) Coronal sectional (upper panel) and axial sectional (lower panel) images of the left superior PV demonstrating asymmetric stenosis after ablation. The full and dotted lines indicate the diameters of the peri-lesion references and the point of the maximal luminal reduction, respectively. This PV has a 48% luminal reduction in the supero-inferior direction (upper panel), but only a 14% luminal reduction in the antero-posterior direction (lower panel), indicating a heterogeneous pattern of stenosis in this vein. (C) Measurement of the left atrial diameters. The transverse (full line), antero-posterior (dotted line), and longitudinal diameters (arrow) were measured.*

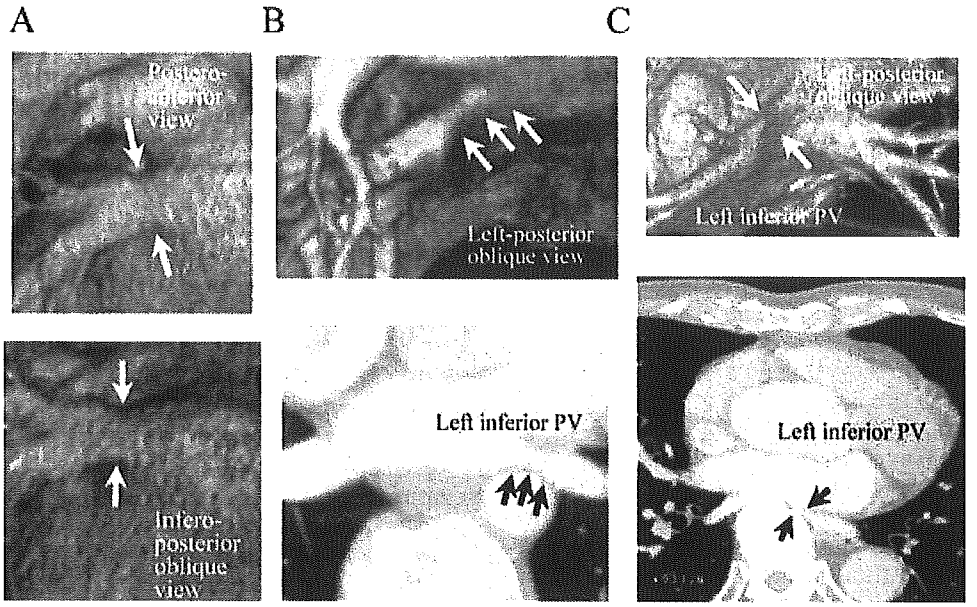

Figure 2. *(A) Volume rendering images of the left inferior pulmonary vein (PV) in a patient with atrial fibrillation before ablation. The arrows indicate a narrowing of the vein (27% luminal reduction). (B) A volume rendering image postprocessing cutting the descending aorta (upper panel) and curved MPR (lower panel) of the left inferior PV before ablation. Dominant luminal reduction on the posterior side is shown. (C) A volume rendering image of the left inferior PV postprocessing cutting the spine (upper panel) and axial cross-sectional CT image (lower panel) in a control patient. The arrows indicate the narrowest portion of the vein (66% luminal reduction). A narrowed and kinked left inferior PV, positioned between the left atrium and the spine, is shown (black arrows).*

carefully selected cross-sectional source images, and orthogonal to the source images.[9]

Measurements and Analysis

In 30 patients with AF, quantitative measurements of the PVs, using electronic three-dimensional digital calipers, were performed in the right superior (n = 30; RS), right inferior (n = 30; RI), left superior (n = 26; LS), and left inferior (n = 26; LI) PVs (Fig. 1). Four obvious left common PVs and three right middle PVs that were found were excluded from the analysis. The PV ostial diameter was measured in two orthogonal directions (antero-posterior and supero-inferior directions; Fig. 1A). One of the ends of the digital caliper was set at the geometric junction (i.e., inflection or apex of the parabolic outline) between the PV and the intervenal bridging wall for the supero-inferior measurement or anterior wall of the left atrium (LA) or LA appendage for the antero-posterior measurement (Fig. 1A). The intersection of the opposite wall with a line perpendicular to

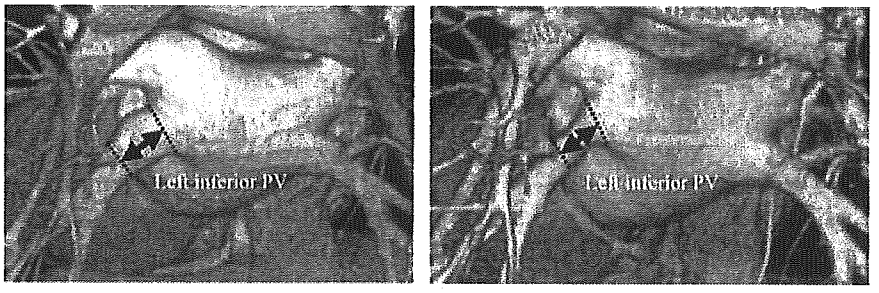

Figure 3. *Volume rendering images of the left inferior pulmonary vein (PV) before (left panel) and after ablation (right panel). The trunk length of the PV shortened after ablation (23% reduction compared with that before ablation).*

the trunk axis running from the aforementioned junction was used as the other end for the measurement (Fig. 1A).

When a luminal reduction inside the PV was visualized on the curved MPR image, the severity of the luminal reduction was assessed as the percent diameter reduction inside the PV with a referential diameter that was the average of the distal and proximal peri-lesion diameters (Fig. 1B). After measuring the luminal reduction in two orthogonal directions, the larger of the percent diameter reduction values was used as the severity of the luminal reduction.We set 0% for the percent diameter reduction of the PVs without a luminal reduction. A luminal reduction $\geq$25% was defined as PV narrowing. We distinguished a *de novo* luminal reduction in the ablated PV from the pre-existent luminal reduction that was visualized both before and after ablation using the bidirectional curved MPR. In the PV without a pre-existent luminal reduction, we determined the luminal reduction that could be visualized after ablation to be a *de novo* luminal reduction. In the PVs with a pre-existent luminal reduction, an alteration $\geq$2 mm in the distance from the PV ostium to the narrowest point, conversion to tandem lesions from a single lesion, conversion to a bidirectional lesion from a unidirectional lesion, or increase $\geq$15% in the luminal reduction was defined as emergence of a *de novo* luminal reduction. The narrowest portion of the *de novo* luminal reduction was defined as the ablation site. The distance between the estimated ablation site and the PV ostium before ablation was calculated as (distance between the point of the maximal diameter reduction and the PV ostium $\times$ length of the PV trunk before ablation/length of the PV trunk after ablation). The diameter of the estimated ablation site before ablation was measured on the first CT image. The percent change in the diameter of the ablation site also was calculated as (100 – 100 $\times$ diameter of the ablation site after ablation/diameter of the estimated ablation site before ablation).

The length of the PV trunk, which was defined as the distance from the ostium to the first branching point of the PV, was measured in the coronal sectional view (Fig. 1A). The antero-posterior, supero-inferior, and transverse diameters of the LA were also measured before and after ablation (Fig. 1C). The transverse diameter of the LA was measured between the ostia of the superior PVs on the oblique coronal section. The antero-posterior diameter was measured at the level of the sino-tubular junction on the oblique sagittal section. The longitudinal diameter was measured from the roof to the mitral annulus on the oblique sagittal section. The percent diameter reduction of the PV ostium and LA was calculated as (100 – 100 $\times$ diameter before ablation/diameter after ablation).

All ablation sites were verified using multiplane fluoroscopy, and each ablation site was assessed using the 12 divided segments of the PV wall (Fig. 4A), and the extent of the circumferential ablation area and number of RF energy deliveries in the four anatomic segments of the PV (superior, inferior, anterior, and posterior segments; Fig. 4B) were obtained.

Statistical Analysis

Continuous variables are expressed as mean $\pm$ SD. Continuous variables were compared with the *t*-test or one-way ANOVA coupled with Scheffe's test, as appropriate. Categorical variables were compared using the Fisher's exact test. Correlations between variables were assessed by Pearson's linear correlation and tested using Fisher's *z* transformation. All statistical analyses were carried out using the Stat-View statistical package, version 5.0 (Abacus Concept, Inc., Berkeley, CA, USA). A P value < 0.05 was considered statistically significant.

Results

PV and LA Characteristics in Patients with AF Before Ablation

The supero-inferior diameter of the PV ostium was greater than the antero-posterior ostial diameter in each of the PVs ($P < 0.0001$ for each; Table I). The supero-inferior ostial diameter did not differ among the four PVs, but the antero-posterior ostial diameter of the LIPV was smaller than the other three PVs ($P < 0.05$ for each). The supero-inferior and antero-posterior diameters of the ostium in the AF patients were greater than those in the control subjects (Table I). However, the trunk length of each PV in the AF patients (12.9 $\pm$ 7.6 mm) did not differ from the control subjects (11.9 $\pm$ 7.4 mm, $P = 0.4$). The transverse and antero-posterior LA diameters were greater in the AF patients than in the control subjects (Table I).

Luminal Reduction of the PVs Before Ablation

A luminal reduction in the PVs was observed in patients with AF before ablation as well as in the control subjects. In patients with AF, the average luminal reduction of all 112 PVs that were assessed was 6 $\pm$ 10% (range, 0–34), and the distance from the ostium to the narrowest point in the PV was 6.7 $\pm$ 3.9 mm in the supero-inferior direction and 7.1 $\pm$ 4.6 mm in the antero-posterior direction. A luminal reduction was frequently observed and its severity was the greatest in the LIPV among the four PVs (Table II). PV narrowing was found in nine (8%) PVs (eight LIPVs and one LSPV; Table II,

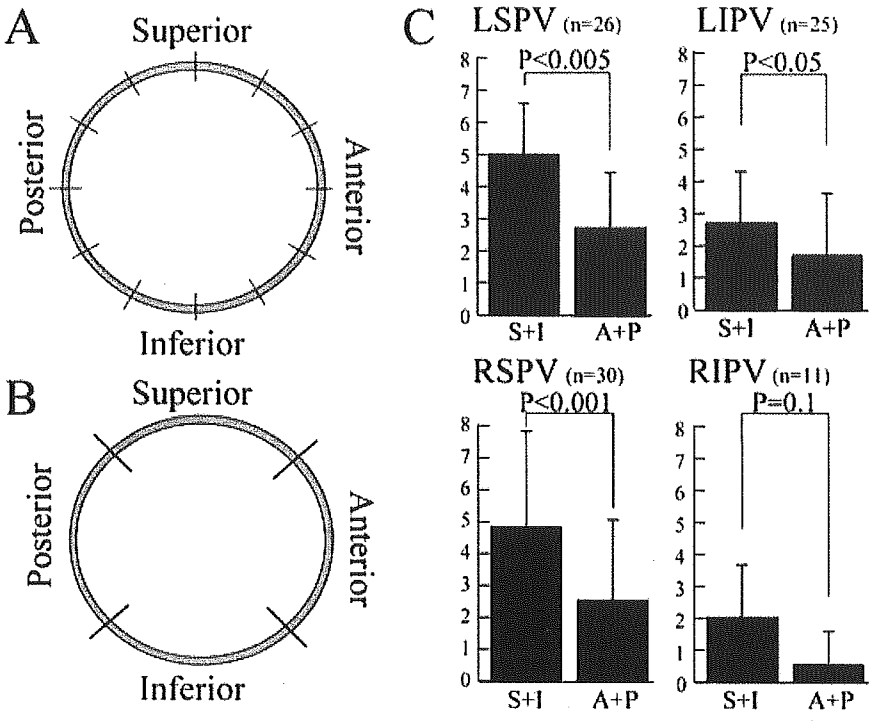

Figure 4. *(A) A representation of the pulmonary vein (PV) divided into 12 segments for calculating the circumferential ablation region. (B) A representation of the PV divided into four segments to assess the number of RF energy deliveries at the four anatomic segments of the PV. (C) Total number of RF energy applications at the superior and inferior segments (S + I) and at the anterior and posterior (A + P) segments within the PV. LI (S) = left inferior (superior); RI (S) = right inferior (superior).*

Fig. 2A and B). Four of the PV narrowings (44%) were found only in the antero-posterior direction, but no PV narrowings were found only in the supero-inferior direction.

In the control subjects, the average luminal reduction was 5.8 ± 13% (range, 0–66%), and PV narrowing was found in six LIPVs (10%). A control subject with mild pectus excavatum had a 66% luminal reduction (Fig. 2C). There were no differences in the incidence or severity of segmental PV narrowing between the AF patients and the control subjects. Inside the LIPVs, six of the eight narrowings (75%) in the AF patients and four of the six narrowings (67%) in the control subjects were dominant on the posterior side adjacent to the descending aorta (Fig. 2B).

Ablation Procedure

RF energy was delivered at the 92 PVs (30 RSPVs, 11 RIPVs, 26 LSPVs, and 25 LIPVs) and complete electrical isolation was achieved in 88 (96%) PVs. In each of the PVs, RF energy was delivered more often at the superior and inferior segments than at the anterior and posterior segments (Table III, Fig. 4C). No complications occurred during the ablation procedures.

Status of the Patients up to the Time of the Second CT

After ablation, 18 patients (60%) had no AF recurrence without the use of antiarrhythmic drugs. In the remaining 12 patients (40%), AF recurred within 1 week after ablation, and they were treated with class I or class III antiarrhythmic drugs that had been ineffective before ablation and they subsequently had no symptomatic AF episodes. No patients had any symptoms from the PV narrowing. At the second CT scanning, no patients had varied ≥5% in the ratio of the "R-to-P interval" to the "R-to-R interval" compared to the first scanning.

Luminal Reduction Inside the PV After Catheter Ablation

After PV isolation, a *de novo* luminal reduction was present in 53 ablated PVs (58%; range, 5–46%), and the average severity of the *de novo* luminal reduction in all 92 ablated PVs, including 39 PVs with no *de novo* luminal reduction (severity = 0%), was 16 ± 14%. The percent diameter reduction of the *de novo* luminal reduction was greater in the supero-inferior direction (14 ±

Table I.

Measured Diameters of the Pulmonary Vein Ostia and Left Atrium in Patients with Atrial Fibrillation and Control Subjects

A. Pulmonary Vein	AF Patients Before Ablation	Ablated PVs of the AF patients		Control Subjects	P Value 1	P Value 2
		Before	After			
LSPV Number	26		26	15		
Supero-inferior diameter (mm)	21.1 ± 3.0	21.1 ± 3.0	18.7 ± 2.9	20.1 ± 3.1	<0.0001	0.3
Antero-posterior diameter (mm)	17.2 ± 2.9	17.2 ± 2.9	15.3 ± 2.6	15.1 ± 2.8	<0.0001	<0.05
SI/AP	1.24 ± 0.17	1.24 ± 0.17	1.24 ± 0.16	1.35 ± 0.17	0.8	0.07
RSPV Number	30		30	15		
Supero-inferior diameter (mm)	21.6 ± 2.7	21.6 ± 2.7	17.6 ± 2.8	19.7 ± 2.9	<0.0001	<0.05
Antero-posterior diameter (mm)	17.7 ± 2.8	17.7 ± 2.8	16.3 ± 2.6	15.5 ± 2.6	<0.001	<0.05
SI/AP	1.24 ± 0.33	1.24 ± 0.33	1.22 ± 0.20	1.28 ± 0.19	0.4	0.5
LIPV Number	26		25	15		
Supero-inferior diameter (mm)	20.6 ± 3.1	20.5 ± 3.1	18.9 ± 3.0	18.2 ± 2.9	<0.0005	<0.05
Antero-posterior diameter (mm)	14.9 ± 2.8	14.9 ± 2.8	13.9 ± 2.5	12.8 ± 3.0	<0.0005	<0.05
SI/AP	1.37 ± 0.18	1.37 ± 0.18	1.39 ± 0.20	1.50 ± 0.29	0.8	0.3
RIPV Number	30		11	15		
Supero-inferior diameter (mm)	20.4 ± 2.8	19.8 ± 2.2	19.3 ± 1.8	19.1 ± 2.5	0.2	0.1
Antero-posterior diameter (mm)	16.4 ± 2.3	17.0 ± 1.5	16.4 ± 1.6	14.3 ± 2.6	0.06	<0.01
SI/AP	1.26 ± 0.18	1.17 ± 0.16	1.18 ± 0.16	1.39 ± 0.37	0.6	0.09

B. Left Atrium	Control Subjects	AF Patients		P Value 1	P Value 2
		Before	After		
Number	15	30			
Traverse diameter (mm)	48.0 ± 5.0	55.6 ± 6.8	53.2 ± 6.2	<0.0005	<0.001
Longitudinal diameter (mm)	64.0 ± 7.5	66.1 ± 7.9	63.9 ± 8.6	<0.005	0.4
Antero-posterior diameter (mm)	31.7 ± 6.2	37.7 ± 7.7	35.6 ± 7.6	<0.0001	<0.05

Values are mean ± standard deviation. AF = atrial fibrillation; LI (S) = left inferior (superior); PV = pulmonary vein; RI(S) = right inferior (superior); SI/AP = ratio of supero-inferior diameter to antero-posterior diameter. p value 1: before ablation vs. after ablation (paired t test), p value 2: the AF patients before PV isolation vs. the control subjects (non-paired t test).

12%) than in the antero-posterior direction (9 ± 13%, P < 0.0001; Table II and Figs. 1B and 5), but the severity of the PV stenosis in the antero-posterior direction was greater than in the supero-inferior direction in 14% of ablated PVs. *De novo* PV narrowing after ablation was found in 24 PVs (26%; Table II). It could be detected in both directions in 10 PVs (42%), but was detected only in the supero-inferior direction in the remaining 14 PVs (58%; Fig. 1B). No *de novo* PV narrowing was found only in the antero-posterior direction. Four PVs which had PV narrowing before ablation demonstrated *de novo* PV narrowing after ablation. These were all LIPVs, and it occurred at a proximal site to the site with pre-existent PV narrowing in three LIPVs and at the site with pre-existent PV narrowing in the remaining one LIPV.

The severity of the *de novo* luminal reduction was greater and the incidence of the *de novo* narrowing was higher in the left PVs than the right PVs, and the LIPV had the greatest severity of luminal reduction and the highest incidence of *de novo* narrowing among the four PVs (Table II). The distance between the PV ostium and the site showing the maximal diameter reduction of the *de novo* luminal reduction was 6.0 ± 3.3 and 5.6 ± 3.2 mm in the coronal and axial sectional views, respectively. The distance between the distal and proximal referential points (length of the luminal reduction) was 9.7 ± 2.2 mm in the supero-inferior direction and 9.8 ± 2.1 mm in the antero-posterior direction.

Diameter Reduction at the Ostium of the PV After Catheter Ablation

In the LSPV, RSPV, and LIPV, the supero-inferior and antero-posterior diameters of the PV ostium after ablation were smaller than those

Table II.

Percent Diameter Reduction and Its Severity for the Pulmonary Veins and the Incidence of the Narrowing of the Pulmonary Vein Before and After Ablation

	%Diameter Reduction		Severity (%)	Incidence of PV Narrowing (%)
	Supero-Inferior	Antero-Posterior		
Preexistent luminal reduction before ablation				
LSPV	3.7 ± 7.4	2.0 ± 6.0	4.4 ± 7.9	1/26 (4%)
RSPV	2.1 ± 5.4	0 ± 0	2.1 ± 5.4	0/30 (0%)
LIPV	8.0 ± 11.0	11.7 ± 13.6	16.0 ± 12.3†	8/26 (31%)*
RIPV	0.7 ± 4.0	0.9 ± 5.2	1.7 ± 6.4	0/30 (0%)
De novo luminal reduction after ablation				
LSPV	18.5 ± 10.0	10.8 ± 11.5	19.6 ± 10.5	9/26 (35%)
RSPV	10.1 ± 11.1	3.0 ± 6.6	10.3 ± 11.0	3/30 (10%)
LIPV	20.4 ± 12.9	18.4 ± 15.3	24.5 ± 14.0	12/25 (48%)
RIPV	1.1 ± 3.8	0 ± 0	1.1 ± 3.8	0/11 (0%)

Values are mean ± standard deviation. After measurement of the %diameter reduction in two orthogonal directions (supero-inferior and antero-posterior directions), the greater value for the %diameter reduction was chosen for a severity of luminal reduction. LI (S) = left inferior (superior); PV = pulmonary vein; RI (S) = right inferior (superior). *P < 0.05, †P < 0.005, ‡P < 0.0005.

before ablation (P < 0.001 for all; Table I). Both the supero-inferior and antero-posterior percent diameter reductions in the PV ostium correlated with the severity of the *de novo* luminal reduction (r = 0.31, P < 0.01 and r = 0.30, P < 0.01, respectively). In the 20 non-ablated PVs (19 RIPVs and 1 LIPV), both diameters of the PV ostium after ablation were also smaller than those before ablation (Fig. 6A).

Longitudinal Shrinkage of the Ablated PVs

In the ablated PVs, the PV trunk after ablation (12.2 ± 7.6 mm) was shorter than before ablation (13.4 ± 8.1 mm, P < 0.0001; Figs. 3 and 6B). The average percent shortening of the PV trunk was 8.4 ± 10.2% (range, −5% to 34%). Shortening of the PV trunk correlated with the severity of the *de novo* luminal reduction inside the PV (r = 0.40, P < 0.0005), but it was not related to the percent diameter reduction of the LA (r = 0.15, P = 0.14 for transverse; r = 0.21, P = 0.056 for longitudinal; and r = −0.14, P = 0.22 for antero-posterior percent diameter reduction of the LA). In the non-ablated PVs, the trunk length did not change after ablation (P = 0.07; Fig. 6B).

Table III.

Distribution of the Ablated Area Where RF Energy Was Delivered in the Pulmonary Vein

	Number of RF Energy Application					Ablated Area in the PV	Total Amounts of RF Energy (J)
	Superior	Inferior	Anterior	Posterior	Total		
LSPV	1.9 ± 1.3	3.1 ± 2.0	1.5 ± 1.3	1.2 ± 1.2	7.7 ± 3.3	0.49 ± 0.16	13,617 ± 7,996
RSPV	2.6 ± 1.5	2.3 ± 2.1	1.2 ± 1.5	1.3 ± 1.3	7.3 ± 4.6	0.50 ± 0.15	13,301 ± 6,552
LIPV	1.7 ± 1.2	1.1 ± 1.2	0.8 ± 1.1	0.8 ± 1.3	4.4 ± 2.9	0.39 ± 0.22	6,246 ± 4,285
RIPV	1.3 ± 1.4	0.8 ± 1.0	0.1 ± 0.4	0.4 ± 0.7	2.5 ± 1.3	0.26 ± 0.21	3,099 ± 2,510
Total	2.0 ± 1.4	2.1 ± 2.0	4.1 ± 2.7	1.0 ± 1.2	6.2 ± 4.0	0.48 ± 0.50	10,680 ± 7,887

Values are mean ± standard deviation. LI (S) = left inferior (superior); n = number; PV = pulmonary vein; RI(S) = right inferior (superior). *P < 0.05, †P < 0.005, ‡P < 0.0005.

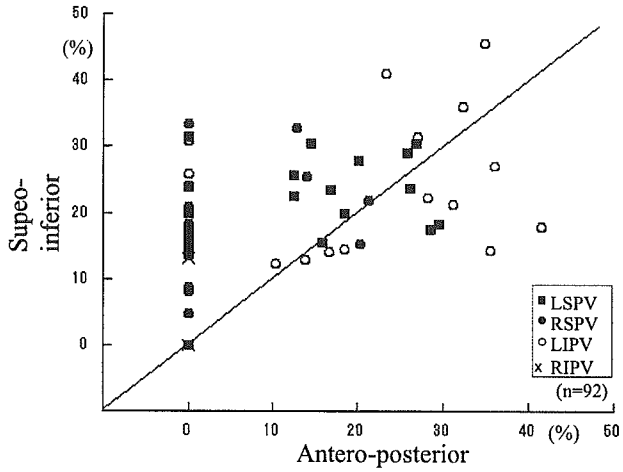

Figure 5. *Relationship between the percent reduction of the supero-inferior diameter and the antero-superior diameter of the PV after ablation. The abbreviations are the same as in Figure 4.*

Changes in the LA and Relationship to the PVs After Ablation

The LA diameters after ablation were smaller than those before ablation ($P < 0.005$, for each; Table I). The supero-inferior percent diameter reduction of the ostium in the ablated PVs ($r = 0.30$, $P < 0.005$), as well as in the nonablated PVs ($r = 0.53$, $P < 0.05$), correlated with the supero-inferior percent diameter reduction of the LA. The reductive luminal alteration at the ablation site derived from the estimated ablation site before ablation (average, 23 ± 15%; range, −5% to 65%) correlated not only with the supero-inferior percent diameter reduction inside the PV ($r = 0.46$; $P < 0.001$) but also with the percent diameter reduction of the LA ($r = 0.43$; $P < 0.001$).

Discussion

Major Findings

The quantitative analysis of the PV morphology performed by CT in this study demonstrated the following novel findings. (1) Shrinkage of the PV trunk was often observed in the ablated PVs, and its severity did not correlate with the changes in the LA diameter but did with the severity of the *de novo* PV narrowing. (2) After ablation, the reduction in the diameters of both the PV ostium and the ablation site in the ablated veins, as well as the reduction in the diameter of the PV ostium in the nonablated PVs, correlated with the reduction in the diameter of the LA after ablation. (3) Luminal reduction inside the PV after ablation occurred in a bidirectional manner, and its severity was usually greater in the supero-inferior direction than in the antero-posterior direction, with 60% of PV narrowing detected only in the supero-inferior direction. No *de novo* PV narrowing had a diameter reduction ≥25% only in the antero-posterior

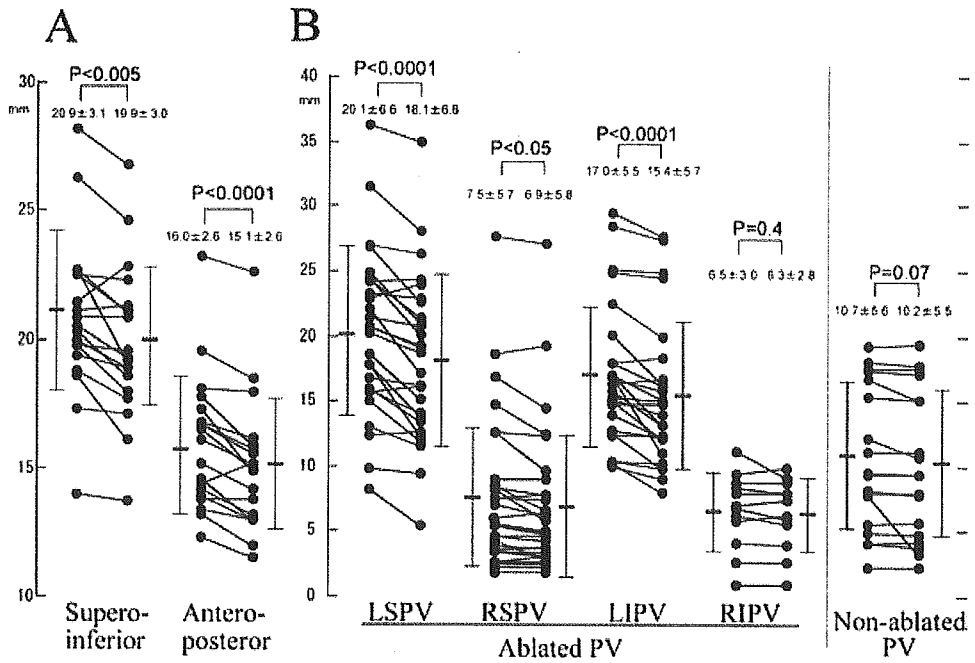

Figure 6. *(A) Changes in the supero-inferior and antero-posterior ostial diameters of the non-ablated pulmonary veins (PVs). (B) Changes in the trunk length of the ablated and non-ablated PVs. The abbreviations are the same as in Figure 4.*

direction. (4) Narrowing of the PV was found in about 10% of PVs in the patients with AF before ablation as well as in the control subjects, and it was most often found in the LIPV. No pre-existent narrowing had a diameter reduction ≥25% only in the supero-inferior direction.

These findings indicate that an asymmetric bidirectional luminal reduction and longitudinal shrinkage of the PV are characteristic morphologic changes after ablation. Structural and reverse remodeling of the PV together with the LA remodeling may affect the changes in the PV diameter. Bidirectional viewing before and after ablation is preferable to avoid missing a pre-existent lesion or underestimating the asymmetric bidirectional reduction within the PV. Meanwhile, only bidirectional viewing after ablation can distinguish a unidirectional narrowing that can be sporadically encountered, between one that is a *de novo* narrowing located only in the supero-inferior direction, and one that is a pre-existent narrowing located only in the antero-posterior direction.

Pattern and Proposed Mechanism of the Morphologic Changes in the PVs After Ablation

A recent study demonstrated that fibrocellular intimal proliferation, endovascular contraction, and elastic proliferation were responsible for PV narrowing more than 6 weeks after RF energy applications, and that endovascular contraction was observed typically at the site at which the RF energy application produced necrosis with a resulting scar formation.[10] In the present study, shrinkage of the PV trunk after ablation was not influenced by the changes in the LA size but by the severity of the PV narrowing at the ablation sites. Therefore, endovascular contraction caused by RF energy deliveries within the proximal portion of the PV might cause a longitudinal shrinkage of the PV trunk as well as PV stenosis.

The muscle sleeve over the proximal portion of the PV is distributed heterogeneously, which is predominantly in the inferior portion of the superior PVs and in the superior portion of the inferior PVs.[11] A recent study also demonstrated that the sites with electrical breakthroughs where RF energy delivery impaired the conduction between the LA and the PV were often located at the superior and inferior segments within the PV.[12] In keeping with a heterogeneous distribution of the myocardial sleeve within the proximal PV and to isolate the PV electrically from the LA, RF energy has to be applied more often at the superior and inferior segments than at the anterior and posterior segments within the PV, which may result in heterogeneous PV stenosis.

Proposed Mechanism of the Narrowing Within the Nonablated PVs

Dense fibrous connective tissue around the distal portion of the myocardial sleeve from the LA into the PV has been reported.[13] We hypothesized that the dense fibrous tissue representing the histological junction between the LA and the proper PV involving medial smooth muscle forms a pre-existent mild luminal reduction in the PV at the vicinity of the ostium. In addition, as Figure 2B shows, adjacency to the descending aorta may be associated with the greatest frequency of narrowing in the LIPV. In patients with pectus excavatum, a kinking of the LIPV has been reported.[14] The specific location of the vein lying between the LA and the spine may be related to the narrowing of the LIPV in this group (Fig. 2C).

Reverse Remodeling After PV Isolation in the PVs and LA

A decrease or elimination of the recurrence of AF has been expected to develop "reverse remodeling" of the LA and PVs, resulting in restoration of the enlarged dimensions. However, few studies have ever characterized the reverse remodeling of the PVs or the relationship between the LA and the PVs after ablation. In the present study, we demonstrated that dilated PV ostia in both non-ablated and ablated PVs are reduced after ablation, and that the reduction in the diameter of the PV ostium correlates with that of the LA after ablation. These findings indicate that reverse remodeling of the PVs can occur after successful ablation and is observed with a reduction in the LA size. In addition to the histological changes caused by the RF energy delivery, reverse remodeling of the PVs may play an important role in the reduction of the diameter at the ablation site after ablation. The present study and a previous study demonstrated no significant difference in the PV trunk between the AF and the control subjects.[7] Meanwhile, Kato et al. reported that the PV trunk of the AF group was significantly larger than that of the control subjects.[5] The difference in the results among the three studies was supposedly due to undisclosed differences in the characteristics, i.e., physical size or gender of the control subjects.

Imaging and Measurements

In previous articles, the severity of the reduction inside the PV was determined quantitatively using a unidirectional view. Further, a measurement or estimation of the diameter at the ablation site before ablation was not sufficiently

attempted.[4–6] The curved MPR is a kind of three-dimensional reconstruction that allows for an integrated oblique view encompassing the whole PV lumen, trunk and branches, and has been available for quantitative evaluation of stenosis of the coronary arteries.[9,15] In the present study, we measured the PV diameters in two orthogonal directions and estimated the diameter at the ablation site in consideration of the longitudinal shrinkage retrospectively using curved MPR.

Limitations

A limitation of this study was that the extensive shrinkage might have complicated the estimation of the luminal reduction or alteration in the PVs because of an underestimation of the reference diameters or deformation of the ostia. A second limitation was that we could not completely distinguish a *de novo* luminal reduction from a pre-existent luminal reduction. Third, in the present study, no clinical stenosis of the PVs occurred after ablation. Thus, we cannot assert whether or not unidirectional viewing missed in any way any clinical PV stenosis after ablation. Finally, the distance between the ablation site and the ostium was calculated on the assumption of a linear relationship between the trunk length and the luminal reduction of the PVs, and this assumption might not have been the case. However, as mentioned in the "Results" section, the percent shortening of the trunk length demonstrated a significant linear relationship to the luminal reduction. Therefore, we believe that the error range was very small and made no difference in the results.

References

1. Haissaguerre M, Shah DC, Jais P, et al. Electrophysiological breakthroughs from the left atrium to the pulmonary veins. Circulation 2000; 102:2463–2465.
2. Oral H, Knight BP, Tada H, et al. Pulmonary vein isolation for paroxysmal and persistent atrial fibrillation. Circulation 2002; 105:1077–1081.
3. Robbins IM, Colvin EV, Doyle TP, et al. Pulmonary vein stenosis after catheter ablation of atrial fibrillation. Circulation 1998; 98:1769–1775.
4. Scharf C, Sneider M, Case I, et al. Anatomy of the pulmonary veins in patients with atrial fibrillation and effects of segmental ostial ablation analyzed by computed tomography. J Cardiovasc Electrophysiol 2003; 14:150–155.
5. Kato R, Lickfett L, Meininger G, et al. Pulmonary vein in patients undergoing catheter ablation of atrial fibrillation: Lessons learned by use of magnetic resonance imaging. Circulation 2003; 107:2004–2010.
6. Dill T, Neumann T, Ekinci O, et al. Pulmonary vein diameter reduction after radiofrequency catheter ablation for paroxysmal atrial fibrillation evaluated by contrast-enhanced three-dimensional magnetic resonance imaging. Circulation 2003; 107:845–850.
7. Schwartzman D, Lacomis J, Wigginton WG. Characterization of left atrium and distal pulmonary vein morphology using multidimensional computed tomography. J Am Coll Cardiol 2003; 41:1349–1357.
8. Tada H, Oral H, Wasmer K, et al. Pulmonary vein isolation: Comparison of bipolar and unipolar electrograms at successful ostial ablation sites. J Cardiovasc Electrophysiol 2002; 13:13–19.
9. Ropers D, Baum U, Pohle K, et al. Detection of coronary artery stenoses with thin-slice multi-detector row spiral computed tomography and multiplanar reconstruction. Circulation 2003; 107:664–666.
10. Taylor GW, Kay GN, Zheng X, et al. Pathological effects of extensive radiofrequency energy applications in the pulmonary veins in dogs. Circulation 2000; 101:1736–1742.
11. Ho SY, Cabrera JA, Tran VH, et al. Architecture of the pulmonary veins: Relevance to radiofrequency ablation. Heart 2001; 86:265–270.
12. Yamane T, Shah DC, Jais P, et al. Electrogram polarity reversal as an additional indicator of breakthroughs from the left atrium to the pulmonary veins. J Am Coll Cardiol 2002; 39:1337–1344.
13. Saito T, Waki K, Becker AE. Left atrial myocardial extension onto pulmonary veins in humans: Anatomic observation relevant for atrial arrhythmias. J Cardiovasc Electrophysiol 2000; 11:888–894.
14. Takahashi K, Sugimoto H, Ohsawa T. Obliteration of the descending aortic interface in pectus excavatum: Correlation with clockwise rotation of the heart. Radiology 1992; 182:825–828.
15. Achenbach S, Ulzheimer S, Baum U, et al. Noninvasive coronary angiography by retrospectively ECG-gated multislice spiral CT. Circulation 2000; 102:2823–2328.

ELSEVIER

International Journal of Cardiology 103 (2005) 105–106

International Journal of Cardiology

www.elsevier.com/locate/ijcard

Letter to the Editor

Large collateral conus branch to the left anterior descending branch of the coronary artery in a subject with angina pectoris demonstrated by multislice computed tomography

Nobusada Funabashi*, Miki Asano, Issei Komuro

Department of Cardiovascular Science and Medicine, Chiba University Graduate School of Medicine, 1-8-1 Inohana, Chuo-ku, Chiba City, Chiba 260-8670, Japan

Received 20 March 2004; accepted 17 June 2004
Available online 5 February 2005

A 70-year-old male presented to our hospital for chest pain. To evaluate the coronary arteries, electrocardiogram-gated enhanced multislice computed tomography (CT) (Light Speed Ultra, General Electric, Milwaukee, WI, USA) was performed with a 1.25-mm slice thickness, helical pitch 3.25. Thirty seconds after intravenous injection of 100 ml of iodinated contrast material (350 mgI/ml), CT scanning was performed with retrospective ECG-gated reconstruction and volume data were transferred to a workstation (Virtual Place Office Azemoto Tokyo Japan).

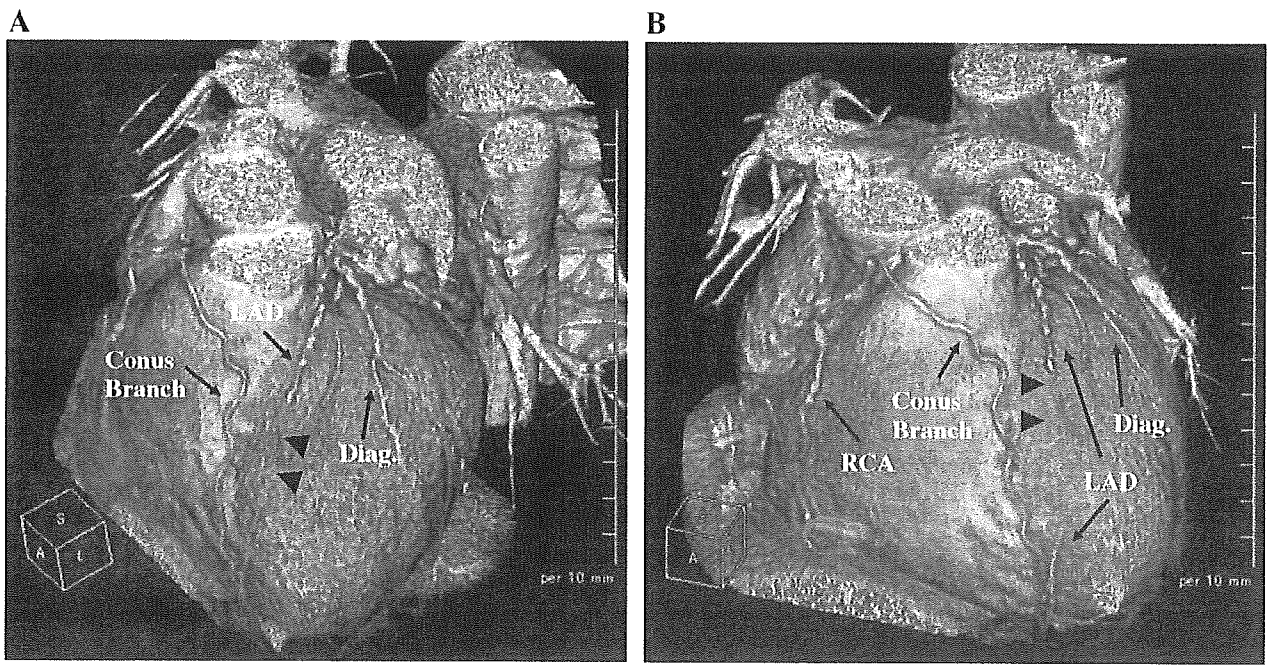

Fig. 1. Three dimensional volume-rendering images of enhanced electrocardiogram-gated multislice computed tomography revealed total occlusion of the left anterior descending branch (LAD) (arrowheads) and a large conus branch originating from the right coronary artery (RCA) that fed into the distal part of the LAD. Diag. indicates diagonal branch.

* Corresponding author.
E-mail address: nobusada@ma.kcom.ne.jp (N. Funabashi).

0167-5273/$ - see front matter
doi:10.1016/j.ijcard.2004.06.017

Three dimensional volume-rendering images revealed total occlusion of the left anterior descending branch (LAD) (arrowheads, Fig. 1A,B) and a large conus branch originating from the right coronary artery (RCA) that fed into the distal part of the LAD. Conventional coronary angiograms revealed the same findings of total occlusion of the LAD (arrowheads, Fig. 2A) and a collateral conus branch originating from the RCA that fed into the distal part of the LAD (Fig. 2B). As blood flow of the collateral artery was good, normal motion of the left ventricle was revealed by a selective left ventriculogram, and his chest pain was improved by the oral administration of nitroglycerin and a β-blocker, no interventions were performed.

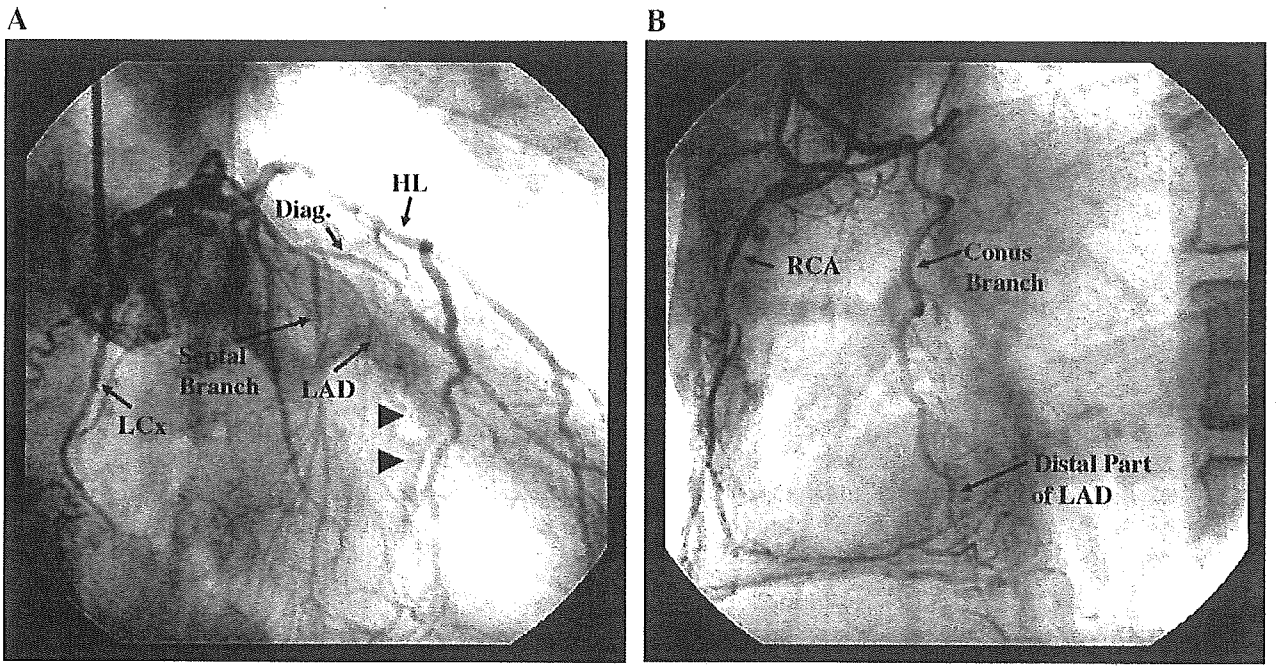

Fig. 2. Conventional coronary angiograms revealed the same findings of total occlusion of the LAD (arrowheads, A) and a collateral conus branch originating from the RCA that fed into the distal part of the LAD (B). Diag., HL, and LCx indicate diagonal branch, high lateral branch, and left circumflex branch, respectively.

ELSEVIER

International Journal of Cardiology 106 (2006) 270–272

International Journal of Cardiology

www.elsevier.com/locate/ijcard

Letter to the Editor

Atherosclerotic right internal thoracic arterial aneurysm demonstrated by multislice computed tomography

Yuriko Niitsuma[b], Nobusada Funabashi[a,*], Mizuho Imamaki[b], Issei Komuro[a], Masaru Miyazaki[b]

[a]*Department of Cardiovascular Science and Medicine, Chiba University Graduate School of Medicine, 1-8-1 Inohana, Chuo-ku, Chiba City, Chiba 260-8670, Japan*

[b]*Department of General Surgery, Chiba University Graduate School of Medicine, Chiba, Japan*

Received 30 October 2004; accepted 31 December 2004
Available online 1 April 2005

Keywords: Internal thoracic arterial aneurysm; Multislice computed tomography; Coronary artery bypass graft

A 74-year-old male presented with weight loss; stomach cancer was diagnosed that required surgery. As he had chest pains on effort, a conventional coronary angiogram was performed, which revealed severe stenosis of the left main branch, and a coronary artery bypass graft (CABG) was indicated.

Evaluation of the aorta and internal thoracic artery (ITA) was done using ECG-gated enhanced multislice computed tomography (CT) (Light Speed Ultra 16, General Electric, Milwaukee, Wisconsin) with a 1.25 mm slice thickness, helical pitch 6.00. CT scanning was performed 30 s after intravenous injection of 100 ml of iodinated contrast material (350 mgI/ml). Axial source (Fig. 1A) and sagittal view (Fig. 1B) of multiplanar reconstruction image and volume-rendered images (Fig. 1C and D), revealed normal findings except for a right ITA (RITA) aneurysm (arrowheads) and aortic arch calcification. The surgeons had planned to connect the left ITA to the left circumflex branch and, as stomach cancer precluded the use of the gastroepiploic artery, they chose the RITA to connect to the left anterior descending (LAD) artery. During the CABG procedure the RITA aneurysm (10 mm in diameter) was resected (arrow Fig. 2A). The radial artery was connected to the proximal portion of the RITA and the radial arterial graft to LAD. Pathological examination of the resected aneurysm revealed plaque (★) with thickened intima, fragmentation of the membrane elastic interna (arrow) (Fig. 2B) and excessive cholesterin deposition in intima. Therefore the RITA aneurysm was considered due to atherosclerosis rather than specific arteritis or systemic connective tissue disease.

* Corresponding author. Tel.: +81 43 222 7171.
E-mail address: nobusada@ma.kcom.ne.jp (N. Funabashi).

0167-5273/$ - see front matter
doi:10.1016/j.ijcard.2004.12.081

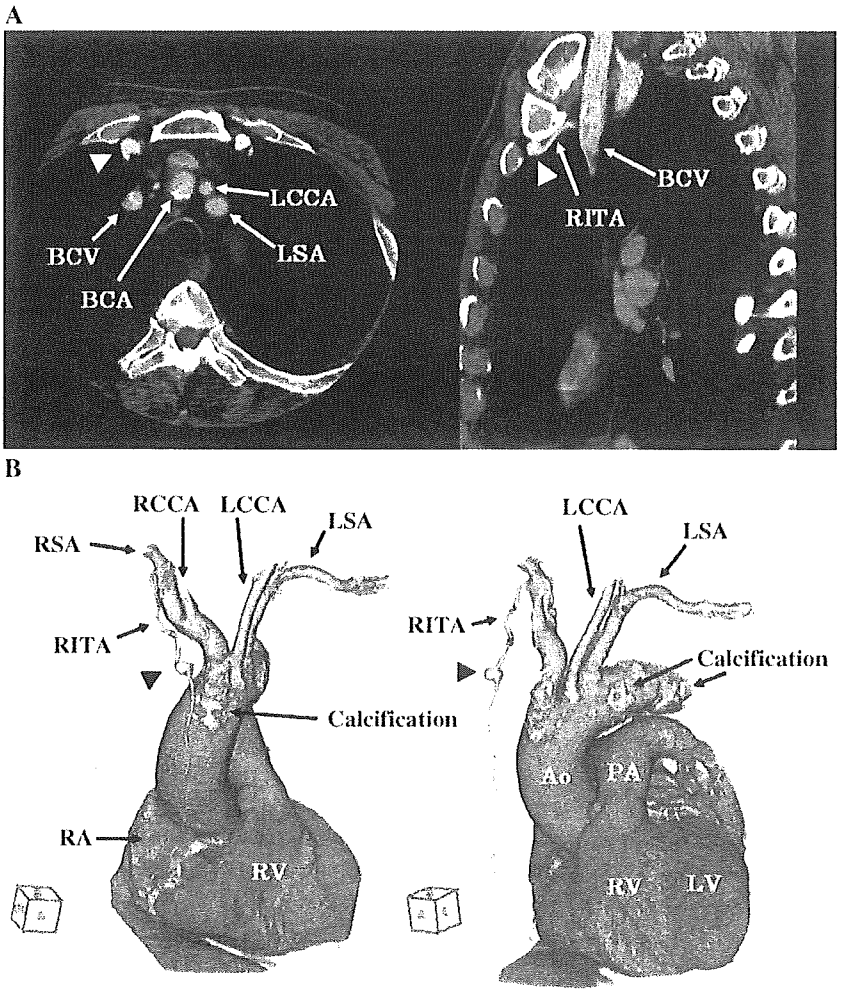

Fig. 1. A and B: Axial source (A) and sagittal view (B) of multiplanar images of enhanced electrocardiograph-gated multislice computed tomography show the aneurysm of the right internal thoracic artery (RITA) (arrowheads). (C) and (D) Volume-rendered images of enhanced electrocardiogram-gated multislice computed tomography show the aneurysm of the right internal thoracic artery (RITA) (arrowheads). Calcification of aortic arch can also be observed. BCV (brachiocephalic vein), BCA (brachiocephalic artery), LCCA (left common carotid artery), LSA (left subclavian artery), RSA (right subclavian artery), RCCA (right common carotid artery), RA (right atria), RV (right ventricle), Ao (aorta), PA (pulmonary artery), and LV (left ventricle).

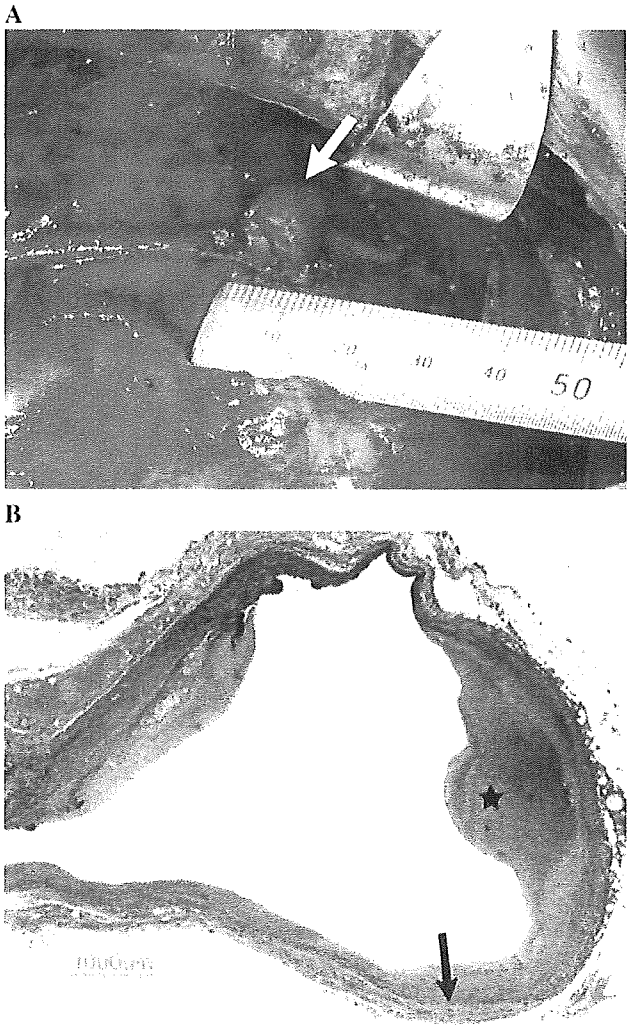

Fig. 2. (A) Intraoperative photograph of the aneurysm of the right internal thoracic artery (RITA) (arrow). (B) Histological section of the wall of the aneurysm of the RITA in Elastica van Gieson stein represented plaque (★) with thickened intima and fragmentation of the membrane elastica interna (arrow). Original magnification ×20.

ELSEVIER

International Journal of Cardiology 107 (2006) 130–131

International Journal of Cardiology

www.elsevier.com/locate/ijcard

Letter to the Editor

Patency of gastroepiploic arterial graft to left circumflex branch with distal portion of the anastomotic site demonstrated by multislice computed tomography

Nobusada Funabashi*, Issei Komuro

Department of Cardiovascular Science and Medicine, Chiba University Graduate School of Medicine, Chiba University Hospital, 1-8-1 Inohana, Chuo-ku, Chiba City, Chiba 260-8670, Japan

Received 2 January 2005; accepted 6 January 2005
Available online 5 April 2005

A 77-year-old male presented to our hospital with chest pain on effort 5 years previously. Conventional coronary angiogram (CAG) revealed occlusion in the proximal left circumflex branch (LCx) and right coronary artery (RCA), with distal collateral arteries and occlusion of the ostium of the left subclavian artery (LSA). He underwent a coronary artery bypass connecting the aortic root to the mid portions of the RCA using a saphenous vein graft (SVG), and a gastroepiploic arterial (GEA) graft to the distal LCx. An artificial graft was also implanted from the ascending aorta to the mid portion of the LSA. Postoperatively, CAG revealed a patent GEA graft but completely occluded ostium of the SVG. Five years later, although asymptomatic, electrocardiogram (ECG)-gated enhanced multislice computed tomography (CT) (Light Speed Ultra 16, General Electric, Milwaukee, WI) was performed with 1.25-mm slice thickness, helical pitch 6.00. Thirty seconds after intravenous injection of 100 ml of iodinated contrast material (350 mg/ml), CT scanning was performed with retrospective ECG-gated reconstruction and volume data were transferred to a workstation (Virtual Place Office Azemoto, Tokyo).

Volume-rendered images revealed occlusion of the LSA and patent mid and distal portions fed by the artificial graft (Fig. 1A,B). The SVG was completely occluded at the ostium. The proximal LCx was occluded and the distal portion of the anastomotic site of the GEA graft was visualized (arrowheads Fig. 2A,B), findings identical to the previous CAG.

* Corresponding author.
E-mail address: nobusada@ma.kcom.ne.jp (N. Funabashi).

0167-5273/$ - see front matter
doi:10.1016/j.ijcard.2005.01.049

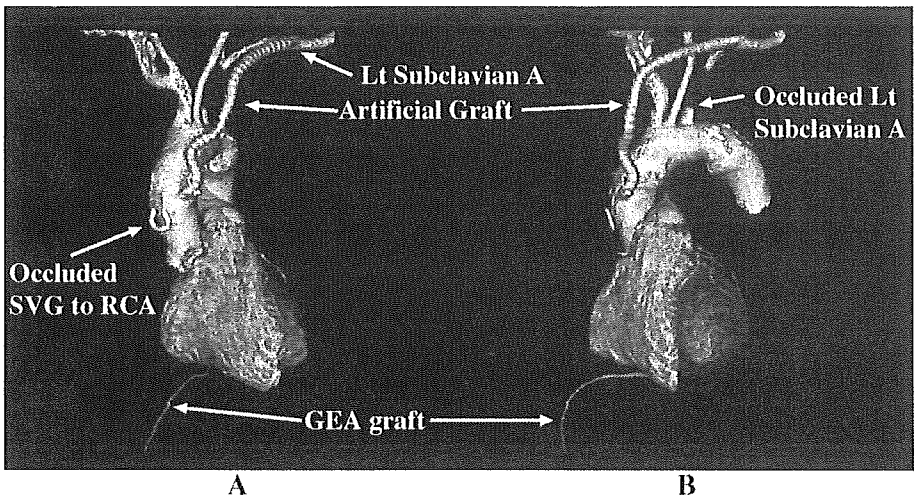

Fig. 1. Volume-rendered images of enhanced ECG-gated multislice computed tomography from the anterior view (A) and left anterior view (B) revealed the occluded proximal portion of the left subclavian artery (Lt Subclavian A), and the mid and distal portions of the Lt Subclavian A fed by the artificial graft from the ascending aorta with good patency. The saphenous vein graft (SVG), which should have connected to the right coronary artery (RCA), was completely occluded at the ostium of the graft. The gastroepiploic arterial (GEA) graft could also be visualized.

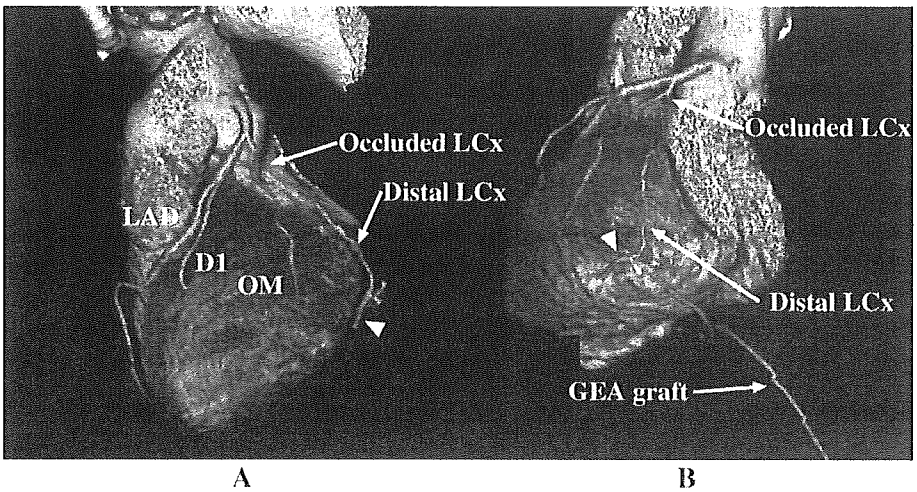

Fig. 2. Volume-rendered images of enhanced ECG-gated multislice computed tomography from the left superior posterior view (A) and posterior view (B) revealed that the proximal portion of the left circumflex branch (LCx) was occluded. The GEA graft was connected to the distal portion of the LCx and the distal portion of the anastomotic site of the GEA graft was visualized (Arrowheads). LAD, D1, and OM indicate left anterior descending branch, 1st diagonal branch, and obtuse marginal branch, respectively.

Available online at www.sciencedirect.com

SCIENCE DIRECT®

Genomics 86 (2005) 127 – 141

GENOMICS

www.elsevier.com/locate/ygeno

Interpreting expression profiles of cancers by genome-wide survey of breadth of expression in normal tissues☆

Xijin Ge[a,b,*], Shogo Yamamoto[a], Shuichi Tsutsumi[a], Yutaka Midorikawa[a], Sigeo Ihara[a], San Ming Wang[b], Hiroyuki Aburatani[a,c,*]

[a]*Genome Science Division, Research Center for Advanced Science and Technology, The University of Tokyo, 4-6-1 Komaba, Meguro-ku, Tokyo 153-8904, Japan*

[b]*Center for Functional Genomics, ENH Research Institute, Northwestern University Feinberg School of Medicine, 1001 University Place, Evanston, IL 60201, USA*

[c]*CREST, Japan Science and Technology Corporation (JST), Japan*

Received 9 November 2004; accepted 12 April 2005
Available online 9 June 2005

Abstract

A critical and difficult part of studying cancer with DNA microarrays is data interpretation. Besides the need for data analysis algorithms, integration of additional information about genes might be useful. We performed genome-wide expression profiling of 36 types of normal human tissues and identified 2503 tissue-specific genes. We then systematically studied the expression of these genes in cancers by reanalyzing a large collection of published DNA microarray datasets. We observed that the expression level of liver-specific genes in hepatocellular carcinoma (HCC) correlates with the clinically defined degree of tumor differentiation. Through unsupervised clustering of tissue-specific genes differentially expressed in tumors, we extracted expression patterns that are characteristic of individual cell types, uncovering differences in cell lineage among tumor subtypes. We were able to detect the expression signature of hepatoctyes in HCC, neuron cells in medulloblastoma, glia cells in glioma, basal and luminal epithelial cells in breast tumors, and various cell types in lung cancer samples. We also demonstrated that tissue-specific expression signatures are useful in locating the origin of metastatic tumors. Our study shows that integration of each gene's breadth of expression (BOE) in normal tissues is important for biological interpretation of the expression profiles of cancers in terms of tumor differentiation, cell lineage, and metastasis.

Keywords: Tissue-specific gene; Tumor differentiation; DNA microarray data interpretation; Breadth of expression; BRCA1; ESR1

Introduction

Genome-wide expression profiling with DNA microarrays has been widely used to identify new cancer subtypes and expression signatures associated with prognosis [1–5]. The expression data of thousands of tumor samples, each characterized by the expression levels of up to ~40,000 transcripts, are being quickly accumulated in the public repositories (reviewed in [6]). Due to technological limitations and the inherent complexity of the gene regulatory mechanism, such data are often noisy and extremely multivariate, leading to difficulties in data interpretation.

Besides the need for robust computational tools, integration of additional biological information about genes is essential for uncovering molecular mechanisms underling expression profiles. For example, functional categories from the Gene Ontology (GO) consortium [7], KEGG databases of molecular interaction pathways [8], and genome sequences of promoters are playing important roles in understanding a cluster of genes defined by expression profiling. In this paper, we introduce another kind of information that

☆ DNA microarray data from this article have been deposited with NCBI Gene Expression Omnibus (GEO) under accession: GSE2361.

* Corresponding authors. Hiroyuki Aburatani is to be contacted at Genome Science Division, RCAST, The University of Tokyo, 4-6-1 Komaba, Meguro-ku, Tokyo 153-8904, Japan. Fax: +81 3 5452 5355. Xijin Ge is to be contacted at ENHRI, 1001 University Place, Evanston, IL 60201, USA. Fax: +1 224 364 5003.

E-mail addresses: haburata-tky@umin.ac.jp (H. Aburatani), xge@northwestern.edu (X.J. Ge).

0888-7543/$ - see front matter © 2005 Elsevier Inc. All rights reserved.
doi:10.1016/j.ygeno.2005.04.008

concerns each gene's expression pattern in a panel of normal tissues.

Only a small portion of the 30,000–40,000 protein-coding genes [9,10] in the human genome are essential to the survival of individual cells, hence are constitutively expressed in different types of tissues [11]. Transcription of most genes is regulated by a cell differentiation process, and thus is often highly variable among tissue/cell types and developmental stages. While ubiquitously expressed genes (so-called maintenance genes [11]) play key roles in basic cellular processes, tissue-specific genes are related to the functioning of particular organs. Although it is still difficult to obtain expression profiles for individual cell types that constitute normal organs, genome-wide expression profiles of bulk tissues has been carried out by serial analysis of gene expression (SAGE) and DNA microarrays [11–17]. For each gene, such studies define its breadth of expression (BOE) in normal tissues, which tell where a certain gene is expressed under normal physiological conditions. Categorization of genes based on BOE might serve as additional sources of information to help us decipher the complex expression profiles observed in cancers.

In this paper, we performed additional microarray experiments of normal tissues to search extensively for tissue-specific genes and then systematically reanalyzed previously published DNA microarray data of various cancers. We employed oligonucleotide microarrays to measure the expression of ~20,000 transcripts in 3 fetal and 33 adult normal human tissues (full list is given in Fig. 1A). Pooled RNA samples are used to maximize tissue coverage, which is important for defining tissue specificity. We retrieved data from a collection of previously published datasets of liver, brain, breast, and lung cancers. Then we focused on the genes that are specifically expressed in certain normal tissues but are differentially expressed in tumors arising from the same anatomical sites. Our strategy is to create a small but carefully selected dataset of normal tissue gene expression profiles, and use it as a seed to reanalyze large datasets in the public domain.

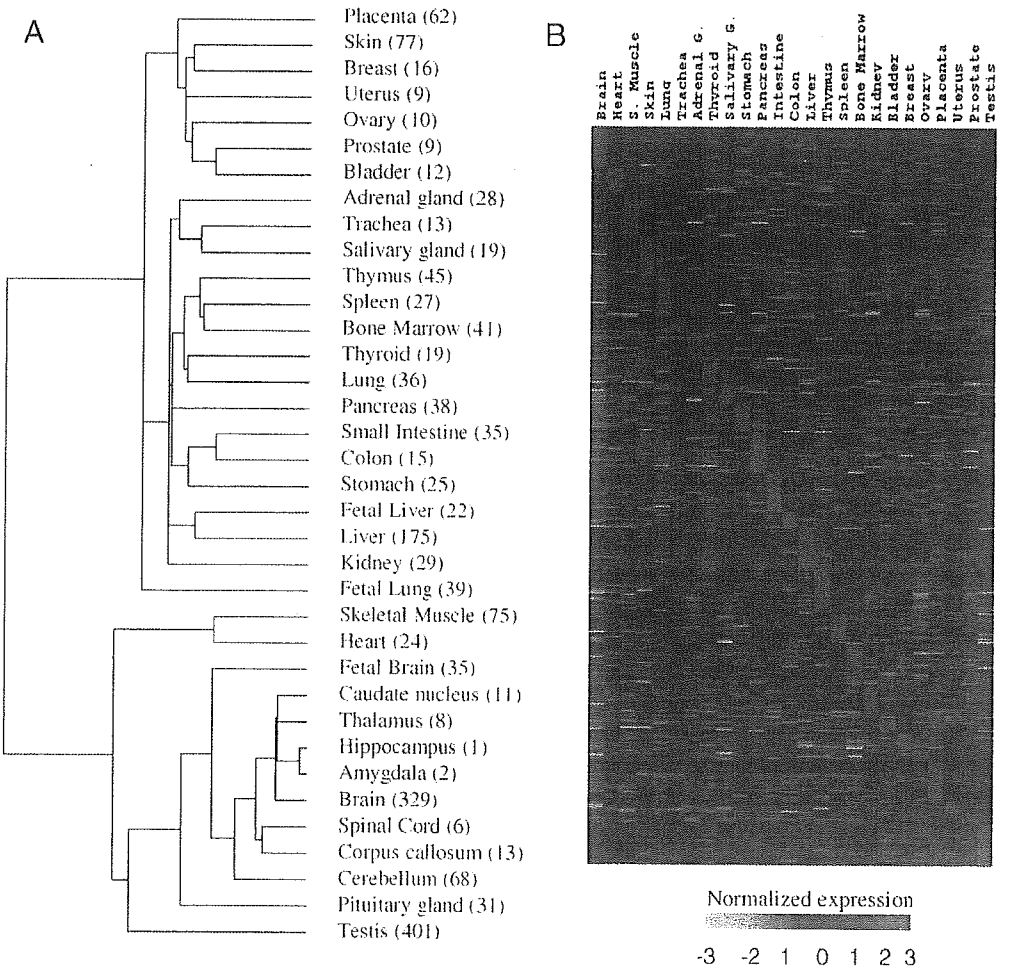

Fig. 1. (A) Hierarchical clustering of gene expression data of 36 types of normal human tissues. Data for 7396 genes are used to generate the cluster tree. Numbers in brackets indicate the number of tissue-specific genes. (B) Expression pattern of tissue-specific genes. Red denotes high expression and green low expression. Only the top 40 with highest specificity are shown for each tissue.

Results

Expression profiling of normal tissues

Using the Affymetrix U133A array, we performed expression profiles of 36 common normal human tissues, each represented by a pooled RNA sample (see Supplementary Information for details). The raw data are available at our web site: http://www.genome.rcast.u-tokyo.ac.jp/normal/, and can also be queried through a graphical web interface at http://www.lsbm.org. After eliminating genes with little variation (max/min > 2, max−min > 100, see Method for details) in their expression among tissues, we performed hierarchical clustering of the remaining 7396 probe sets. The result is shown in Fig. 1A. As expected, whole brain, brain regions, fetal brain, and spinal cord form a group related to the nervous system. Other closely related organs also aggregate, such as {colon, small intestine, stomach}, {heart, skeletal muscle}, {skin, breast} etc. The hierarchical tree of different tissues defined by expression patterns might reflect the intrinsic similarities between these tissues as a result of development.

Tissue-specific genes

We identified 1956 probe sets showing exclusively high expression in one of the 36 tissues (see Method for details). These probes map to 1687 UniGene clusters. The number of tissue-specific genes associated with each tissue is also given in Fig. 1A. The expression patterns of these genes are shown in Fig. 1B. Only the top 40 genes with highest Z scores are given. A full list of these genes can be found in the Supplementary Information and our web site http://www.genome.rcast.u-tokyo.ac.jp/normal/. We identified 401 testis-specific genes, 329 brain-specific genes, and 175 liver-specific genes. The remaining tissues have much fewer specific genes. For example, less than 20 are found for trachea, breast, colon, bladder, prostate, ovary, and uterus. This can be understood from the fact these tissues are less specialized and more similar to each other in their physiological organization.

We also identified 920 "tissue-selective" transcripts that are highly expressed in several related tissues (see Method for details). Unlike tissue-specific genes, tissue-selective genes are highly expressed in multiple tissues. For example, we identified 25 genes whose expression is restricted to colon and small intestine, 10 for heart and skeletal muscle, 9 for kidney and liver, 10 for brain and testis, etc. These 920 tissue-selective genes represent 816 UniGene clusters. A full list is available in the Supplementary Information and at our web site http://www.genome.rcast.u-tokyo.ac.jp/normal/. Together with the 1687 tissue-specific genes, we identified 2503 genes whose expression is strongly associated with specific tissues.

Ideally, multiple independent biological replicates representing each tissue type are needed to obtain a robust set of tissue-specific genes. Also more tissue types need to be covered to better define expression specificity. But due to the difficulty in obtaining normal samples we used commercially available pooled RNA. Because of such limitations in the resultant data and our empirical selection criteria, our lists of tissue-specific genes might be subject to false positive and false negative errors. This should be taken into account when using these lists for data interpretation. We reasoned that although tissue specificity of individual genes might be unreliable, it should still be possible to use these lists in a statistical sense by observing the coexpression of a group of such genes.

To validate our list of tissue-specific genes, we used the HuGe Index database [13], which contains biological replicates for some tissues. As shown in Supplementary Fig. 4, tissue-specific expressions of most of these genes can be seen in the HuGe Index database. A similar agreement with the Gene Expression Atlas database [15] is also observed (Supplementary Fig. 5). This agreement between independent datasets supports the effectiveness of sample pooling in our study and the reliability of our lists of tissue-specific genes.

In the following sections we study the expression of these tissue-specific genes in various cancers, starting from simple univariant liver cancer to multivariant lung tumors.

Hepatocyte-specific expression signature and differentiation of liver cancer

It is known that tumor cells sometimes could be transformed into a less differentiated state via a dedifferentiation process [22]. At the molecular level, one would expect the expression of tissue-specific genes to be decreased or lost. To confirm this, we reanalyzed a dataset of hepatocellular carcinoma (HCC) [23], which contains the data of 8 normal liver and 25 HCC samples. The cancer samples are further classified into three categories, namely well-differentiated ($N = 8$), moderately differentiated ($N = 12$), and poorly differentiated ($N = 5$). The expression levels of 12,600 transcripts are obtained with U95A oligonucleotide arrays (Affymetrix, Santa Clara, CA). Of the 175 liver-specific genes identified in the U133A array, 141 are covered by U95A arrays. So we retrieved expression data of these 141 transcripts.

We noted that 9 (6.4%) of these transcripts are often called "absent" in at least 4 normal liver samples, and hence do not show consistent tissue specificity. But the majority (129, or 75%) of these transcripts are called "present" in all of the 8 normal liver samples. When the expressions of these transcripts in other tissues are examined, only 5% (7/141) are all present in 17 normal lung samples [28]. Instead, 72% (102/141) are called absent in at least 80% of the normal lung samples. Even for those that are called present in both tissues, their expression levels in liver are on average 13.5 times higher. Similarly 77% (109/141) of these genes are called absent in at least 80% of normal prostate samples in another microarray datasets [29]. This assured us again the consistency of tissue specificity of the majority of these genes.

We also included 19 transcripts that are specifically expressed in fetal liver. After eliminating some genes with a

variation filter (max−min > 100, max/min > 2), we performed unsupervised clustering analysis with the remaining 64 transcripts. As shown in Fig. 2A, except Cluster γ, we observed a general tendency of increased levels of expression of these transcripts in the order of poorly, moderately, and well-differentiated tumor. Well-differentiated HCC samples are found to form a subcluster characterized by high expression of liver-specific genes. The remaining samples are further divided into two smaller groups, one dominated by poorly differentiated samples and the other moderately differentiated samples. Samples are arranged in the cluster tree according to their degree of differentiation.

Such classification is difficult if we analyze the expression of all genes in the microarray. For comparison, hierarchical clustering with the 3536 of 12,000 transcripts passed a variation filter is shown in Supplementary Fig. 6. Poorly differentiated HCC samples could also be distinguished, but unsupervised global analysis failed to distinguish moderately differentiated from well-differentiated HCC. This is further confirmed by a receiver operating characteristic (ROC) curve given in Fig. 2B. We applied a *k*-nearest neighbor (*k*NN) algorithm [30] to classify samples into well, moderate, or poorly differentiated HCC. We first used the 64 liver-specific transcripts and then all 3536 genes. Using a series of thresholds of percentage vote for making positive predictions, we observed the specificity and sensitivity of prediction in leave-one-out cross-validation. The ROC curve suggests that without further supervised gene selection the list of 64 liver-specific transcripts outperforms the global expression profiles for the classification of samples by degrees of differentiation. This is because these samples are greatly variable in other clinicopathological parameters, such as sex, age, viral infection, invasiveness, etc. By focusing on liver-specific genes, we are able to filter other factors and gain information about tumor differentiation with a higher signal-to-noise ratio.

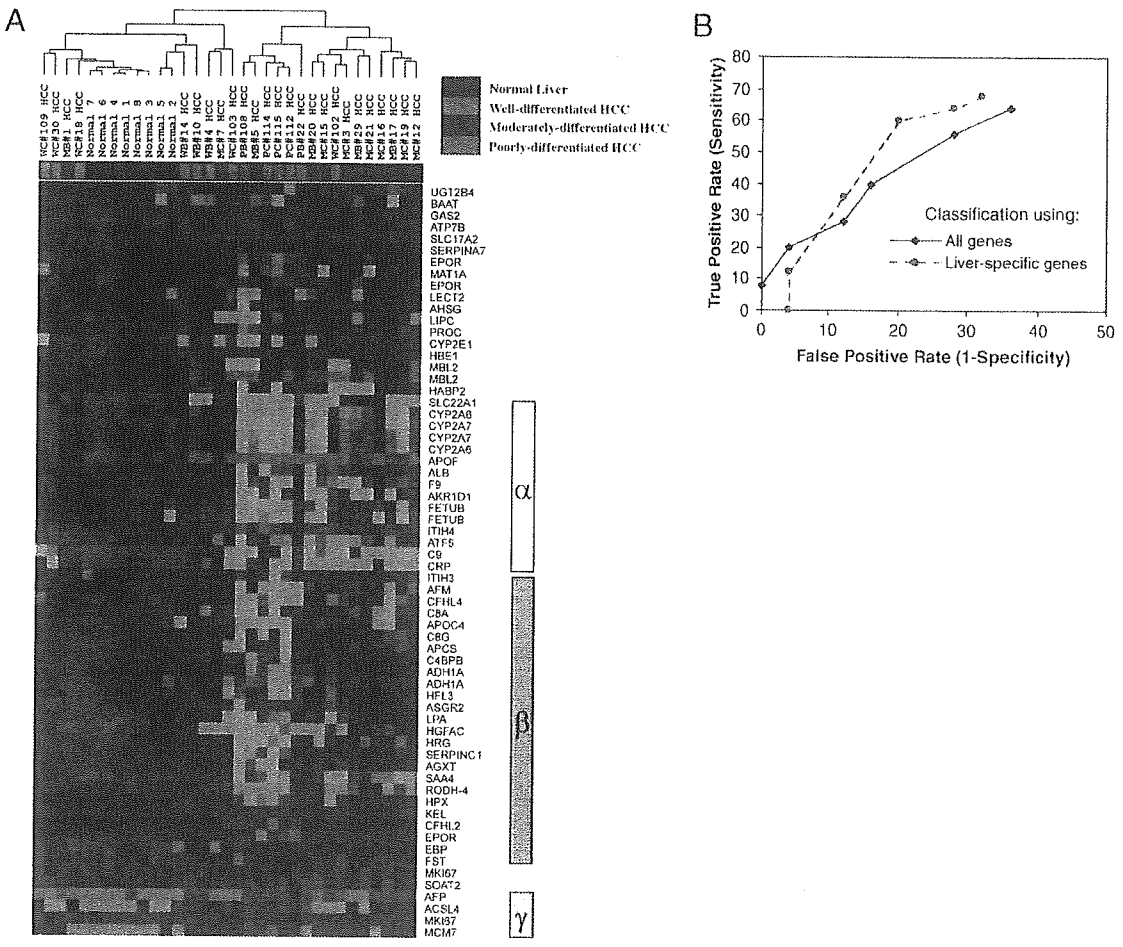

Fig. 2. (A) Unsupervised clustering analysis of a hepatocellular carcinoma (HCC) dataset using liver-specific genes. Well-differentiated HCC (green) and normal liver samples (black) form a subcluster characterized by high expression of liver-specific genes. The remaining samples are further divided into two smaller groups, one dominated by poorly (red) and the other moderately differentiated HCC (blue). While genes in Group α are underexpressed in both moderately and poorly differentiated HCCs, those in Group β show a tendency of increased expression according to degrees of tumor differentiation. Genes in Group γ are overexpressed in poorly differentiated HCC samples. This group includes some fetal-liver specific genes. (B) ROC curve showing that liver-specific transcripts outperform the whole gene set in classifying tumor into well, moderate, or poorly differentiated HCC.